

Coherent control of a few-channel hole type gatemon qubit

Han Zheng,^{1,*} Luk Yi Cheung,¹ Nikunj Sangwan,¹ Artem Kononov,¹ Roy Haller,¹ Joost Ridderbos,² Carlo Ciaccia,¹ Jann Hinnerk Ungerer,¹ Ang Li,³ Erik P.A.M. Bakkers,³ Andreas Baumgartner,^{1,4,†} and Christian Schönenberger^{1,4,‡}

¹*Quantum- and Nanoelectronics Lab, Department of Physics, University of Basel, 4056 Basel, Switzerland*

²*MESA+ Institute for Nanotechnology University of Twente, 7500 AE Enschede, The Netherlands*

³*Department of Applied Physics, Eindhoven University of Technology, 5600 MB Eindhoven, The Netherlands*

⁴*Swiss Nanoscience Institute, University of Basel, 4056 Basel, Switzerland*

(Dated: December 12, 2023)

Gatemon qubits are the electrically tunable cousins of superconducting transmon qubits. In this work, we demonstrate the full coherent control of a gatemon qubit based on hole carriers in a Ge/Si core/shell nanowire, with the longest coherence times in group IV material gatemons to date. The key to these results is a high-quality Josephson junction obtained in a straightforward and reproducible annealing technique. We demonstrate that the transport through the narrow junctions is dominated by only two quantum channels, with transparencies up to unity. This novel qubit platform holds great promise for quantum information applications, not only because it incorporates technologically relevant materials, but also because it provides new opportunities, like an ultra-strong spin-orbit coupling in the few-channel regime of Josephson junctions.

INTRODUCTION

Quantum computing has become a topic of intense activity due to its potential to revolutionize information processing [1]. Presently, one of the most popular platforms are superconducting circuits in the form of transmon qubits, which are already employed in solving noisy intermediate-scale quantum problems [2–4]. Conventional transmons rely on metallic superconductor-insulator-superconductor (SIS) tunnel junctions, in which tuning the qubit frequency requires a magnetic flux in a SQUID geometry [5]. However, flux cross-talk between qubits and the heat load due to the flux control currents are problematic for scaling up the number of qubits [6].

An alternative to metallic transmons are semiconductor-superconductor (Sm-S) hybrid systems [7], so-called gatemon qubits [8, 9], with a wealth of recently demonstrated related concepts, like parity protected qubits [10], gate-tunable fluxonium qubits [11], gatemons operated with only a few highly transparent quantum channels [12, 13], or Andreev level [14–16] and Andreev spin qubits [17–20]. All these devices rely on high-quality crystals with near-perfect Sm-S interfaces. This has limited the material choice mainly to InAs-based systems, like vertically-grown InAs NWs [8, 9, 13, 21, 22], InAs 2D systems [23], or selective-area-grown InAs NWs [24]. However, III/V materials are difficult to integrate in standard CMOS technologies, and hyperfine interactions introduce additional decoherence.

More suitable for CMOS technology would be group IV materials, but only very few gatemon-related experiments have been reported so far: on carbon-nanotubes [25], graphene [26], and large-diameter Ge/Si core/shell NWs [27], with the corresponding qubit coherence times

more than an order of magnitude shorter than in III/V materials. However, improvements are expected, especially for the technologically relevant CMOS compatible Si and Ge systems [28, 29]. In particular, Ge is of increasing interest for quantum information processing [30], because hole states in Ge have a p-wave symmetry, inherently reducing hyperfine interactions, with further improvements expected from isotopic purification. Even more promising might be Ge/Si core/shell nanowires with a 1D hole gas strongly confined by the Ge/Si interface [31, 32] and an electrically tunable, very large “direct” Rashba spin-orbit interaction [33, 34].

In this work, we report the full functionality of a gatemon qubit based on narrow Ge/Si core/shell NWs. The key step is the fabrication of highly transparent Josephson junctions (JJs), in an undemanding ex-situ annealing step [35, 36] driving a thermally activated propagation of superconducting aluminum into the Ge NW core [37–39]. We incorporate such JJs in a gatemon qubit device and explicitly demonstrate the electrical tunability of the qubit frequency and the full coherent control of the qubit in the time domain, with an energy relaxation time on par with III/V systems. Most importantly, these experiments allow us to analyse the qubit anharmonicity, suggesting that the supercurrent through the junction is dominated by two ballistic, virtually Schottky-barrier free conductance channels. This work establishes narrow Ge/Si core/shell NWs as a promising Sm-S hybrid platform for quantum information processing, and opens new avenues to investigate novel effects, for example, in circuit-quantum-electrodynamics (circuit QED) experiments on NWs [40, 41] with ultra-strong spin-orbit interactions.

DEVICE

Our gatemon qubit can be understood as a non-linear LC oscillator that consists of a gate-tunable Ge/Si core/shell NW JJ as the non-linear inductance, depicted in Fig. 1a, and a shunt capacitor C_{qb} shown in Fig. 1b. The NW has a diameter of ~ 20 nm, and is expected to have minimal strain-induced defects and a high carrier mobility due to the [110] growth direction [32]. Such a NW was transferred to an undoped Si/SiO₂ substrate using a micro-manipulator, and contacted by Al using standard lift-off techniques. The crucial step in forming the highly transparent JJ is a thermal annealing step at 200 °C, which drives an inter-diffusion process of Al atoms from the contacts into the Ge core, yielding an Al-Ge-Al junction with an atomically sharp interface [38]. The Si shell remains intact during this process. The bright NW segment in the electron micrograph of Fig. 1a has a Ge core, while the Al-filled segments show a darker contrast. The length of the Ge segment can be controlled by the annealing time, and directly read off as 33 nm for this specific device. The interface between Al and Ge turns out to be highly transparent, since it allows for

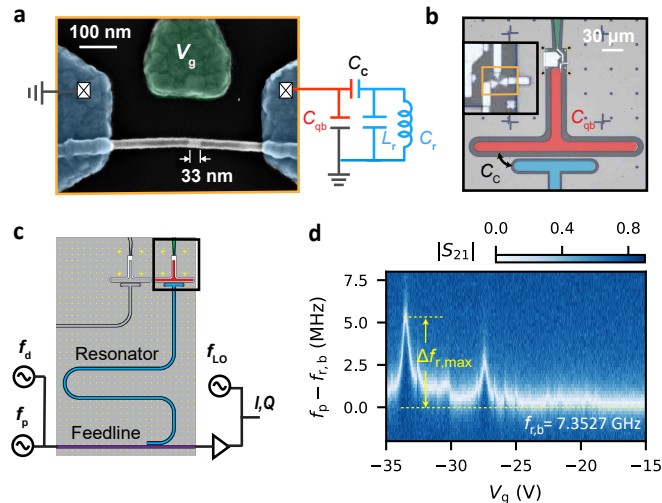


FIG. 1. **Ge/Si core/shell nanowire based gatemon device.** **a**, False-colored SEM image of the Al-Ge-Al junction. The bright segment of the NW has a Ge core, while the dark segments contains Al. The side gate for electrical qubit control is colored in green. The readout resonator is shown as a simplified equivalent circuit on the right. **b**, False-colored optical micrograph of a nanowire Josephson junction shunted by a T-shaped capacitor (red) to the surrounding ground plane and capacitively coupled (C_c) to a superconducting $\lambda/4$ resonator (blue). **c**, Overview of the circuit QED chip and schematic of the readout and control circuit. The $\lambda/4$ resonator is inductively coupled to a feedline for readout. **d**, Transmission amplitude $|S_{21}|$ through the feedline as a function of the gate voltage V_g and the probe frequency f_p , plotted as the difference from the bare resonator frequency $f_{r,b}$. A bright signal difference signifies the resonator frequency f_r .

coherent transport of Cooper pairs through the semiconducting Ge, resulting in a JJ [37, 42]. The Josephson energy E_J can be tuned by a side gate voltage V_g .

The gatemon shunt capacitance C_{qb} (red) is provided by a T-shaped NbTiN island etched into the surrounding ground plane, as shown in Fig. 1b. From electromagnetic simulations, we estimate $C_{\text{qb}} \approx 78$ fF. The island is galvanically connected to the JJ, forming the non-linear LC-oscillator, with the lowest two oscillator states forming the qubit states $|0\rangle$ and $|1\rangle$. The corresponding qubit frequency is determined by the gate tunable Josephson energy E_J and the charging energy $E_c = e^2/2C_{\text{qb}} \approx h \cdot 248$ MHz. The charging energy is fixed and designed to be much smaller than the typical Josephson energy, which significantly reduces the sensitivity to charge noise [43]. In addition, we deposited a 100 nm thick Al layer on the surrounding NbTiN ground plane as a quasiparticle trap (see SI Fig. S1).

An overview of the circuit QED chip is shown in Fig. 1c. The qubit state is probed via a capacitively coupled $\lambda/4$ coplanar transmission line resonator. The short end of the microwave resonator with a current anti-node is inductively coupled to the feedline, while the open end with a voltage anti-node is capacitively coupled to the qubit island, forming the qubit-resonator coupling capacitance C_c . This device was measured in a dilution refrigerator with a base temperature of 15 mK, with consistent results in three different cooldowns.

MEASUREMENTS

Gate tunable qubit frequency with a two-channel Josephson junction

Readout and manipulation of the gatemon qubit is accomplished using standard circuit QED techniques. When the qubit frequency f_q is strongly detuned from the resonator frequency f_r , the system is in the dispersive regime [44]. The qubit then causes a shift Δf_r of the resonator frequency from its bare value $f_{r,b}$, where $\Delta f_r = f_r - f_{r,b} \approx (g/2\pi)^2 / (f_{r,b} - f_q)$ is determined by the qubit-resonator coupling strength g . Figure 1d shows a measurement of the low power transmission amplitude $|S_{21}|$ plotted as a function of the gate voltage V_g and the probe frequency f_p , plotted as the difference from the bare resonator frequency $f_{r,b}$. The minimum in the transmission signal occurs whenever the probe frequency f_p is resonant with f_r .

The bare resonator frequency $f_{r,b} = 7.3527$ GHz can be directly found at gate voltages $V_g > -15$ V, where the semiconducting part of the NW is close to depletion, so that the Josephson current is negligible and the resonator frequency exhibits no shift. The corresponding internal quality factor of $Q_i \approx 2.41 \times 10^5$ is found by simultaneously fitting the resonator transmission amplitude and

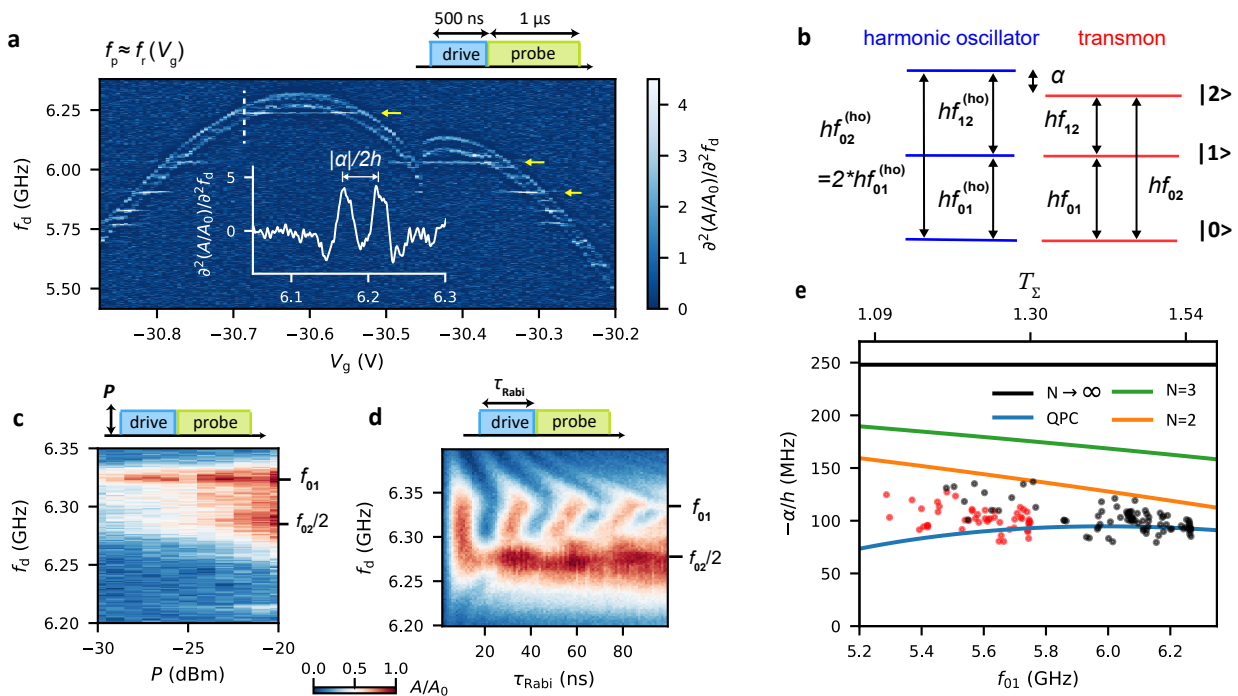


FIG. 2. **Qubit spectroscopy and anharmonicity.** **a**, Second derivative of the normalized resonator response A/A_0 with respect to f_d in a two-tone spectroscopy experiment as a function of the f_d and V_g . The pulse sequence is shown schematically on the top right. The drive power P is set to -20 dBm and the probe frequency close to the resonator frequency f_r . The inset shows a cross section at $V_g = -30.7$ V, clearly showing two peaks. **b**, Energy diagram of a transmon qubit showing explicitly the anharmonicity α . **c,d**, Normalized resonator response A/A_0 in a two-tone spectroscopy experiment as a function of the drive frequency f_d and the drive power P , and as a function of f_d and the drive pulse duration τ_{Rabi} , respectively. The latter exhibits characteristic Rabi oscillations. **e**, Anharmonicity extracted from two-tone spectroscopy experiments, plotted as a function of the qubit frequency f_{01} . The black data points were extracted from **a**, while the red stem from larger gate voltages (around $V_g \approx -20$ V). The top axis labelled T_Σ is obtained directly from the qubit frequency. The solid lines depict anharmonicity inferred from different models (see main text).

phase in the vicinity of $f_{r,b}$ [45]. At lower gate voltages, the hole density in the Ge segment is increased, resulting in a larger Josephson current on the order of a few tens of nA through the JJ, with a correspondingly larger Josephson energy and an increased qubit frequency. The resonator frequency is Lamb-shifted to higher values accordingly, with a maximum of $\Delta f_{r,\text{max}} \approx 6$ MHz found at $V_g \approx -33$ V, pointed out in Fig. 1d. The dispersive shift is positive, suggesting a qubit frequency lower than the bare resonator frequency in this gate voltage range. Δf_r does not increase monotonically with gate voltage, possibly due to resonances in the semiconducting NW section [42]. We also find discontinuities in f_r at specific gate voltages, for example at $V_g \approx 30$ V. These, we attribute to a switching of the qubit frequency f_q due to charge traps in the vicinity of the NW. We note that the resonator frequency shift remains highly reproducible, including the switching, within a gate voltage range of a few volts, but becomes less reproducible when subjected to a wider gate sweep, probably due to rearrangements of such localized charges [22].

To study the quantised energy levels of the device, we perform pulsed two-tone spectroscopy. We apply a 500 ns

drive tone at frequency f_d to the feedline, followed by a $1 \mu\text{s}$ probe tone at an optimised frequency of $f_p \approx f_r$ to probe the resonator. We note that we obtain similar results when driving via the side gate. The in-phase I and quadrature Q components of the transmitted probe tone are obtained using heterodyne detection techniques. We plot the normalized amplitude A/A_0 of the complex signal, which depends on the state of the qubit. In order to resolve fine features, we plot the numerically calculated second derivative of A/A_0 with respect to f_d , as shown in Fig. 2a. The raw data can be found in SI Fig. S2. To avoid large charge rearrangement, we focus on the small gate voltage range of ~ 600 mV shown in Fig. 2a, in which the qubit frequency can be tuned between 5.4 GHz and 6.3 GHz, with a typical qubit-resonator coupling factor of $g \approx 47$ MHz. We attribute the reproducible discontinuity in the qubit frequency at $V_g \approx -30.45$ V to a nearby charge trap. We also find several gate-voltage independent sharp resonances indicated by the yellow arrows in Fig. 2a, possibly due to two-level fluctuators more remote from the gate, for example in the SiO_2 substrate, or due to spurious modes in the electromagnetic environment [46].

The main features in Fig. 2a are two resonances, moving almost in parallel with changing V_g , clearly visible in the cross section shown in the inset for $V_g = -30.7$ V. Here, the spacing between the two peaks is ~ 50 MHz. Based on the generic energy diagram for a transmon qubit shown in Fig. 2b, we attribute the higher frequency resonance to the qubit transition at frequency f_{01} between state $|0\rangle$ and $|1\rangle$. As we will show, the lower resonance originates from two-photon processes that drive the transition from state $|0\rangle$ to the second excited state $|2\rangle$.

To explicitly identify these two peaks, we perform two-tone spectroscopy as a function of frequency and power of the drive tone, as plotted in Fig. 2c. At low powers, only a single resonance is found. For large powers, an additional resonance appears at a slightly lower frequency, consistent with a lower probability for higher order two-photon absorption processes. This transition to the second excited state is also found in the Rabi measurement shown in Fig. 2d, where we plot the resonator response as a function of the drive pulse duration τ_{Rabi} and drive frequency f_d . The drive pulse induces periodic Rabi oscillations between the states $|0\rangle$ and $|1\rangle$, resulting in the characteristic Rabi chevron pattern, with the qubit frequency $f_{01} \approx 6.325$ GHz. Again, we find an additional broader feature for longer pulse times at ~ 6.275 GHz, typically attributed to the $f_{02}/2$ resonance [26, 47]. We point out that the Rabi experiments and the power dependence were not taken at the same gate voltage, because of a slight drift over several weeks of measurements.

This level structure now allows us to directly assess the anharmonicity of the gatemon spectrum $\alpha = 2h(f_{02}/2 - f_{01})$, for different gate voltages. The corresponding data are plotted as black and red points as a function of the gate voltage dependent f_{01} in Fig. 2e. We note that for some specific frequencies, spurious resonances hindered us from extracting the peak positions. Details about the data extraction are discussed in the corresponding SI section.

Figure 2e is one of our main results, which we now use to estimate the transmission probability and the number of conducting channels in the NW junction. Since the semiconducting NW segment is very short (33 nm) compared to typical superconducting coherence lengths, the JJ is in the short-junction limit. The Josephson potential is then well described by $U(\hat{\phi}) = -\Delta \sum_i \sqrt{1 - T_i} \sin^2(\hat{\phi}/2)$, where Δ , T_i , and $\hat{\phi}$ are the superconducting gap, the individual channel transparencies, and the phase difference between the left and right Al segments [48]. The gatemon Hamiltonian then reads $\hat{H} = 4E_c \hat{n}^2 + U(\hat{\phi})$, which can be expanded to fourth order in $\hat{\phi}$ around the potential minimum at $\hat{\phi} = 0$, with the non-harmonic terms used as a perturbation to the harmonic oscillator solutions [12]. This procedure yields

$$hf_{01} = \sqrt{8E_c E_J} - E_c \left(1 - \frac{3 \sum_i T_i^2}{4 \sum_i T_i}\right) \quad (1)$$

and

$$\alpha = -E_c \left(1 - \frac{3 \sum_i T_i^2}{4 \sum_i T_i}\right), \quad (2)$$

with the Josephson energy given by the prefactor of the harmonic $\hat{\phi}^2$ -term in the Hamiltonian, $E_J = \frac{\Delta}{4} \sum_i T_i$. Here, we use the gap $\Delta = 210 \mu\text{eV}$ found in DC transport experiments in a control device (see SI Fig. S6). For this device, we estimate $E_J/E_c \gtrsim 80$, so that we can approximate $hf_{01} \approx \sqrt{8E_c E_J}$. Using the numerically simulated E_c and the measured qubit frequency f_{01} , we obtain the total transmission $T_\Sigma := \sum_i T_i = (hf_{01})^2/(2E_c \Delta)$, used as the top axis of Fig. 2e. The measured quantities hf_{01} and α contain T_Σ and $\sum_i T_i^2$, allowing us to estimate the number of channels and the corresponding transmission probabilities. To do this, we consider two limits [12]. First, we assume N channels of equal transparency $\bar{T} = T_\Sigma/N$, yielding the anharmonicity $\alpha = -E_c(1 - \frac{3}{4}T_\Sigma/N)$. Figure 2e shows the cases $N = 2$, $N = 3$ and $N \rightarrow \infty$. This equal-transmission model provides an estimate of the number of active channels, with the case of $N \rightarrow \infty$ giving the SIS tunnel junction limit $\alpha = -E_c$, with many low-transparency channels. All data points lie below the $N = 2$ case, suggesting that at most two channels dominate the JJ transport. The corresponding mean channel transparency is electrically tunable from $\bar{T} \approx 0.55$ to $\bar{T} \approx 0.77$ in this qubit frequency range.

In the second limit, often called the ‘‘quantum point contact (QPC) limit’’, we assume one fully transmitting ($T_I = 1$) and one partially transmitting channel, with a free parameter T_{II} . This limit yields the lowest possible $|\alpha|$ for a given T_Σ . The resulting dependence is shown in Fig. 2e as the blue solid curve. Since this curve captures our data better than the equal-transparency model, we conclude that the annealed Al-Ge-Al JJ carries one highly transparent channel, consistent with the large values up to $T \approx 0.96$ reported in previous DC transport studies on similar JJs [37, 38], and a second channel with a lower transmission, electrically tuned in the range from $T_{II} \approx 0.1$ to $T_{II} \approx 0.54$.

Coherent control

To demonstrate the full functionality of the gatemon qubit, we performed time-domain measurements, namely Rabi oscillations and Ramsey interferometry, and extract the corresponding relaxation and dephasing time. For these measurements, we use a Josephson parametric amplifier (JPA) to enhance the readout signal already at

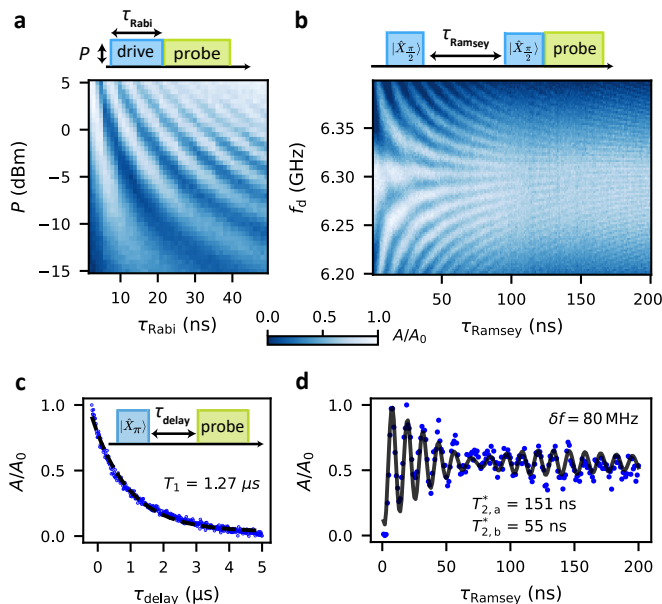


FIG. 3. **Coherent manipulation of the gatemon.** **a**, Rabi oscillations as a function of drive power P and pulse duration τ_{Rabi} , measured at $f_d = 6.345$ GHz and $V_g = -30.7$ V. **b**, Ramsey fringes as a function of drive frequency f_d and time delay t_{Ramsey} measured at $V_g = -30.6$ V. Two $X_{\pi/2}$ pulses separated by τ_{Ramsey} are applied prior to the probe tone. **c**, Measurement of the characteristic energy relaxation time T_1 at $V_g = -30.7$ V. A 10 ns X_π pulse at $P = -10$ dBm drives the qubit into state $|1\rangle$. After a delay time τ_{delay} , the qubit state is readout. The black dashed line shows a fit of an exponential decay, yielding $T_1 = 1.27$ μs . **d**, Ramsey experiment measured at $V_g = -30.6$ V at a detuning of 80 MHz. Two dephasing times of $T_{2,a}^*$ and $T_{2,b}^*$ are extracted by fitting to a double sinusoidal functions with different exponential envelopes.

base temperature [49]. In the following experiments, all pulse sequences start with a common initialisation time of 100 μs to allow the qubit to relax to the ground state $|0\rangle$. We plot the normalized resonator response A/A_0 , which essentially represents the occupation of state $|1\rangle$. Each data point is averaged over 10000 identical pulse sequences.

First, we perform Rabi experiments at a fixed gate voltage V_g and drive at the frequency $f_d \approx f_{01}$. The drive pulse of duration τ_{Rabi} and power P is immediately followed by a 1 μs probe pulse. The drive pulse induces Rabi oscillations between the states $|0\rangle$ and $|1\rangle$ defining the z -axis of a Bloch sphere. The resulting qubit-state dependent resonator response is plotted in Fig. 3a. As expected, the Rabi oscillations become faster for larger drive powers P , which allows for a calibration of the corresponding rotation on the Bloch sphere, around an axis we define as the x -axis. For example, a $X_{\pi/2}$ pulse is obtained as a 5 ns drive pulse at $P = -10$ dBm. We note that we perform these experiments at low powers. If the qubit is driven at larger powers, the two-photon processes

become more probable, resulting in a deviation from the linear dependence of the Rabi frequency on the drive amplitude for $hf_{\text{Rabi}} \gtrsim \alpha$, and a corresponding leakage from the computational space [5], as discussed in SI Fig. S3.

Next, we perform Ramsey interferometry, with the corresponding pulse sequence shown schematically in the upper panel of Fig. 3b. The qubit state vector is first rotated into the xy -plane of the Bloch sphere using a calibrated $X_{\pi/2}$ pulse with the drive frequency f_d slightly detuned from the qubit frequency by $\delta f = f_d - f_{01}$. During a subsequent delay time τ_{Ramsey} , the qubit state precesses around the z -axis of the Bloch sphere, and a phase of $\phi = 2\pi\delta f\tau_{\text{Ramsey}}$ is accumulated. Then the state vector is again rotated by a $\pi/2$ pulse and the qubit occupation read out as a function of ϕ . This results in the Ramsey fringes shown in Fig. 3b, where the resonator response is plotted as a function of f_d and τ_{Ramsey} . The careful timing of these two types of pulses allows one in principle to reach any quantum superposition state on the Bloch sphere.

To quantitatively assess the qubit quality, we now measure the energy relaxation time T_1 and the dephasing time T_2^* . First, to measure T_1 , a X_π pulse is applied to bring the qubit to state $|1\rangle$. After a delay time τ_{delay} , the occupation is measured with a probe pulse. Due to the qubit relaxing to the ground state, the probability of finding the qubit in the excited state decays exponentially over a characteristic time scale of $T_1 = 1.27$ μs . Similarly, we extract the dephasing time T_2^* from a Ramsey measurement at a detuning of $\delta f = 80$ MHz, see Fig. 3d. Instead of the expected single frequency with a dephasing time T_2^* , we find a beating pattern with two slightly different frequencies, similar to the one found in InAs NW gatemons [22] and granular aluminium fluxonium qubits[50]. From a fit to two sinusoidal functions with individual exponential decay times, we obtain the two frequency components $f_{\text{Ramsey},a} = 80.17$ MHz and $f_{\text{Ramsey},b} = 86.05$ MHz. The corresponding time constants are $T_{2,a}^* = 151$ ns and $T_{2,b}^* = 55$ ns. These two frequencies near f_{01} are also found in the high resolution drive power dependent two tone experiments shown in SI Fig. S4. We tentatively attribute the two frequencies to two qubit configurations determined by a nearby low-frequency two-level fluctuator beyond our experimental control. Further qubit characteristics and a discussion of possible physical mechanisms limiting our qubit performance can be found as supplementary information. A comparison between our qubit performance with other gatemons can be found in Fig. S5, which illustrates that our device exhibits the significantly longer gatemon coherence times than previously reported for group IV materials, comparable to recent experiments on InAs platforms.

SUMMARY AND OUTLOOK

In summary, we have demonstrated a fully functional gatemon qubit based on a narrow Ge/Si core/shell nanowire, with a highly transmissive few-channel Josephson junction fabricated using a simple annealing technique, without resorting to sophisticated epitaxial growth techniques. From a detailed analysis of the gatemon anharmonicity, we conclude that the JJ is dominated by two quantum channels with transmissions up to unity. To demonstrate coherent control in the time domain, we performed Rabi and Ramsey interferometry experiments, yielding a T_1 time on par with gatemons in the more established III/V materials. Since we find $T_2^* \ll 2T_1$, the qubit coherence is not limited by the energy relaxation, but rather by dephasing caused by on-chip noise sources [46, 51], suggesting that these times can still be improved significantly.

Our experiments show that Ge/Si core/shell NW gatemons are a competitive platform for electrically tunable superconducting qubits. JJs in the few-channel QPC limit might significantly reduce the charge noise sensitivity as shown in Ref. [52–55], possibly alleviating the requirement for large-footprint capacitors. Ge/Si core/shell NWs also offer additional design parameters not considered for superconducting qubits so far, namely the exceptionally strong and electrically-tunable spin-orbit interaction of the hole carriers, as well as a tunable Landé g -factor [33, 34, 56]. The fabrication techniques and material system employed here are relevant beyond the gatemon qubits. Other platforms, like Andreev spin qubits [17–20] or Andreev level qubits [14–16] will benefit even more from the reduced hyperfine interaction of the hole carriers, and from the sharp, homogeneous interfaces to the Ge islands. Our results opens up new avenues to study Andreev bound states and other, more exotic subgap states in large-spin orbit materials.

ACKNOWLEDGEMENTS

We thank Tom Jennisen for his assistance in optimizing the annealing recipe, Ioan Pop, Patrick Winkel and Thomas Reisinger from Karlsruhe Institute of Technology for providing the Josephson parametric amplifier, and Hugues Pothier, Marcelo Goffman, Bernard van Heck and Vladimir Manucharyan for fruitful and interesting discussions. This research was supported by the Swiss Nanoscience Institute (SNI) and the Swiss National Science Foundation through grants No 172638 and 192027 and through the NCCR-Spin, grant No 180604. We further acknowledge funding from the European Union’s Horizon 2020 research and innovation programme, specifically a) grant agreement 862046, project TOPSQUAD, b) grant agreement No 828948, FET-open project AndQC, and c) grant agreement No 847471,

Marie Skłodowska -Curie, COFUND-QUSTEC.

METHODS

The circuit QED chip was fabricated on an undoped silicon substrate with a 100 nm top thermal oxide, using a combination of optical and electron-beam lithography. After cleaning the wafer, a 68 nm NbTiN film was sputter deposited on the wafer, in which the resonator, feed line and gate line were patterned using optical lithography, and further defined using dry etching in an ICP-RIE process with Ar and Cl₂ gas. Next, we fabricated gold markers to later align the nanowire, and we deposited gold islands (size $\sim 500 \mu\text{m} \cdot 500 \mu\text{m}$) near the borders of the NbTiN film for better thermalization. The resulting resonator quality factors we obtained in fits shown in SI Fig. S7.

The Ge/Si core/shell NWs were then transferred to the circuit QED chip using a micro-manipulator. Source and drain contacts as well as side gates were fabricated using standard electron beam lithography. To remove the native oxide on the Si shell, an 8 s wet etch in buffered HF (buffered oxide etchant 10:1, 4.6% HF) was performed, followed by rinsing in DI water. Next, the chip was immediately loaded into the evaporator where 40 nm of Al was deposited by thermal evaporation. After lift-off, the chip is annealed on a hotplate in ambient at 200°C for 10 min. The NWs were then imaged in a scanning electron microscope to confirm the channel length. Importantly, the annealing and imaging steps can be iterated to obtain the targeted channel length. For each qubit island, we fabricated 3 or 4 annealed junctions, from which we selected the most promising one and connected it to the capacitor and the grounding plane. Ar milling was used to remove the native Al oxide before contacting. The DC and RF wiring of the dilution refrigerator, as well as the measurement setups are discussed in SI Fig. S8.

Author contributions H.Z. and L.Y.C. fabricated the device with help from N.S., A.K., J.R., and J.H.U. H.Z., L.Y.C. and N.S. performed the measurements. C.C. helped measurements with parametric amplifier. H.Z., L.Y.C. and N.S. analyzed the data with inputs from A.K., R.H., A.B. and C.S. A.L. and E.P.A.M.B. conducted the nanowire growth. H.Z. wrote the manuscript with helps from all authors. Project was supervised by A.B. and C.S.

Conflicts of interest The authors declare no conflicts of interest.

Data availability All data in this publication are available in numerical form at: <https://doi.org/10.5281/zenodo.10198946>

- * han.zheng@unibas.ch
 † andreas.baumgartner@unibas.ch
 ‡ christian.schoenberger@unibas.ch
- [1] M. Brooks, Quantum computers: what are they good for?, *Nature* **617**, S1 (2023).
 - [2] J. Preskill, Quantum computing in the nisq era and beyond, *Quantum* **2**, 79 (2018).
 - [3] F. Arute, K. Arya, R. Babbush, D. Bacon, J. C. Bardin, R. Barends, R. Biswas, S. Boixo, F. G. Brandao, D. A. Buell, *et al.*, Quantum supremacy using a programmable superconducting processor, *Nature* **574**, 505 (2019).
 - [4] M. Kjaergaard, M. E. Schwartz, J. Braumüller, P. Krantz, J. I.-J. Wang, S. Gustavsson, and W. D. Oliver, Superconducting qubits: Current state of play, *Annual Review of Condensed Matter Physics* **11**, 369 (2020).
 - [5] P. Krantz, M. Kjaergaard, F. Yan, T. P. Orlando, S. Gustavsson, and W. D. Oliver, A quantum engineer's guide to superconducting qubits, *Applied physics reviews* **6** (2019).
 - [6] S. Krinner, S. Storz, P. Kurpiers, P. Magnard, J. Heinsoo, R. Keller, J. Luetolf, C. Eichler, and A. Wallraff, Engineering cryogenic setups for 100-qubit scale superconducting circuit systems, *EPJ Quantum Technology* **6**, 2 (2019).
 - [7] S. De Franceschi, L. Kouwenhoven, C. Schönberger, and W. Wernsdorfer, Hybrid superconductor–quantum dot devices, *Nature nanotechnology* **5**, 703 (2010).
 - [8] T. W. Larsen, K. D. Petersson, F. Kuemmeth, T. S. Jespersen, P. Krogstrup, J. Nygård, and C. M. Marcus, Semiconductor-nanowire-based superconducting qubit, *Physical review letters* **115**, 127001 (2015).
 - [9] G. De Lange, B. Van Heck, A. Bruno, D. Van Woerkom, A. Geresdi, S. Plissard, E. Bakkers, A. Akhmerov, and L. DiCarlo, Realization of microwave quantum circuits using hybrid superconducting-semiconducting nanowire josephson elements, *Physical review letters* **115**, 127002 (2015).
 - [10] T. W. Larsen, M. E. Gershenson, L. Casparis, A. Kringhøj, N. J. Pearson, R. P. McNeil, F. Kuemmeth, P. Krogstrup, K. D. Petersson, and C. M. Marcus, Parity-protected superconductor-semiconductor qubit, *Physical review letters* **125**, 056801 (2020).
 - [11] M. Pita-Vidal, A. Bargerbos, C.-K. Yang, D. J. Van Woerkom, W. Pfaff, N. Haider, P. Krogstrup, L. P. Kouwenhoven, G. De Lange, and A. Kou, Gate-tunable field-compatible fluxonium, *Physical Review Applied* **14**, 064038 (2020).
 - [12] A. Kringhøj, L. Casparis, M. Hell, T. W. Larsen, F. Kuemmeth, M. Leijnse, K. Flensberg, P. Krogstrup, J. Nygård, K. D. Petersson, *et al.*, Anharmonicity of a superconducting qubit with a few-mode josephson junction, *Physical Review B* **97**, 060508 (2018).
 - [13] A. Danilenko, D. Sabonis, G. W. Winkler, O. Erlandsson, P. Krogstrup, and C. M. Marcus, Few-mode to mesoscopic junctions in gatemon qubits, *Physical Review B* **108**, L020505 (2023).
 - [14] A. Zazunov, V. Shumeiko, E. Bratus, J. Lantz, and G. Wendin, Andreev level qubit, *Physical review letters* **90**, 087003 (2003).
 - [15] C. Janvier, L. Tosi, L. Bretheau, Ç. Girit, M. Stern, P. Bertet, P. Joyez, D. Vion, D. Esteve, M. Goffman, *et al.*, Coherent manipulation of andreev states in superconducting atomic contacts, *Science* **349**, 1199 (2015).
 - [16] L. Cheung, R. Haller, A. Kononov, C. Ciaccia, J. Ungerer, T. Kanne, J. Nygård, P. Winkel, T. Reisinger, I. Pop, *et al.*, Photon-mediated long range coupling of two andreev level qubits, arXiv preprint arXiv:2310.15995 (2023).
 - [17] L. Tosi, C. Metzger, M. Goffman, C. Urbina, H. Pothier, S. Park, A. L. Yeyati, J. Nygård, and P. Krogstrup, Spin-orbit splitting of andreev states revealed by microwave spectroscopy, *Physical Review X* **9**, 011010 (2019).
 - [18] M. Hays, V. Fatemi, K. Serniak, D. Bouman, S. Diamond, G. de Lange, P. Krogstrup, J. Nygård, A. Geresdi, and M. Devoret, Continuous monitoring of a trapped superconducting spin, *Nature Physics* **16**, 1103 (2020).
 - [19] M. Hays, V. Fatemi, D. Bouman, J. Cerrillo, S. Diamond, K. Serniak, T. Connolly, P. Krogstrup, J. Nygård, A. Levy Yeyati, *et al.*, Coherent manipulation of an andreev spin qubit, *Science* **373**, 430 (2021).
 - [20] M. Pita-Vidal, A. Bargerbos, R. Žitko, L. J. Splitthoff, L. Grünhaupt, J. J. Wesdorp, Y. Liu, L. P. Kouwenhoven, R. Aguado, B. van Heck, *et al.*, Direct manipulation of a superconducting spin qubit strongly coupled to a transmon qubit, *Nature Physics* , 1 (2023).
 - [21] L. Casparis, T. Larsen, M. Olsen, F. Kuemmeth, P. Krogstrup, J. Nygård, K. Petersson, and C. Marcus, Gatemon benchmarking and two-qubit operations, *Physical review letters* **116**, 150505 (2016).
 - [22] F. Luthi, T. Stavenga, O. Enzing, A. Bruno, C. Dickel, N. Langford, M. A. Rol, T. S. Jespersen, J. Nygård, P. Krogstrup, *et al.*, Evolution of nanowire transmon qubits and their coherence in a magnetic field, *Physical review letters* **120**, 100502 (2018).
 - [23] L. Casparis, M. R. Connolly, M. Kjaergaard, N. J. Pearson, A. Kringhøj, T. W. Larsen, F. Kuemmeth, T. Wang, C. Thomas, S. Gronin, *et al.*, Superconducting gatemon qubit based on a proximitized two-dimensional electron gas, *Nature nanotechnology* **13**, 915 (2018).
 - [24] A. Hertel, M. Eichinger, L. O. Andersen, D. M. van Zanten, S. Kallatt, P. Scarlino, A. Kringhøj, J. M. Chavez-Garcia, G. C. Gardner, S. Gronin, *et al.*, Gate-tunable transmon using selective-area-grown superconductor-semiconductor hybrid structures on silicon, *Physical Review Applied* **18**, 034042 (2022).
 - [25] M. Mergenthaler, A. Nersisyan, A. Patterson, M. Esposito, A. Baumgartner, C. Schönberger, G. A. D. Briggs, E. A. Laird, and P. J. Leek, Circuit quantum electrodynamics with carbon-nanotube-based superconducting quantum circuits, *Physical Review Applied* **15**, 064050 (2021).
 - [26] J. I.-J. Wang, D. Rodan-Legrain, L. Bretheau, D. L. Campbell, B. Kannan, D. Kim, M. Kjaergaard, P. Krantz, G. O. Samach, F. Yan, *et al.*, Coherent control of a hybrid superconducting circuit made with graphene-based van der waals heterostructures, *Nature nanotechnology* **14**, 120 (2019).
 - [27] E. Zhuo, Z. Lyu, X. Sun, A. Li, B. Li, Z. Ji, J. Fan, E. Bakkers, X. Han, X. Song, *et al.*, Hole-type superconducting gatemon qubit based on ge/si core/shell nanowires, *npj Quantum Information* **9**, 51 (2023).
 - [28] L. C. Gunn III, G. Capellini, M. J. Rattier, and T. J. Pinguet, Methods of incorporating germanium within cmos process (2005), uS Patent 6,887,773.

- [29] M. Veldhorst, H. Eenink, C.-H. Yang, and A. S. Dzurak, Silicon cmos architecture for a spin-based quantum computer, *Nature communications* **8**, 1766 (2017).
- [30] G. Scappucci, C. Kloeffel, F. A. Zwanenburg, D. Loss, M. Myronov, J.-J. Zhang, S. De Franceschi, G. Katsaros, and M. Veldhorst, The germanium quantum information route, *Nature Reviews Materials* **6**, 926 (2021).
- [31] J. Xiang, W. Lu, Y. Hu, Y. Wu, H. Yan, and C. M. Lieber, Ge/si nanowire heterostructures as high-performance field-effect transistors, *nature* **441**, 489 (2006).
- [32] S. Conesa-Boj, A. Li, S. Koelling, M. Brauns, J. Ridderbos, T. T. Nguyen, M. A. Verheijen, P. M. Koentraad, F. A. Zwanenburg, and E. P. Bakkers, Boosting hole mobility in coherently strained [110]-oriented ge-si core-shell nanowires, *Nano letters* **17**, 2259 (2017).
- [33] C. Kloeffel, M. J. Rančić, and D. Loss, Direct rashba spin-orbit interaction in si and ge nanowires with different growth directions, *Physical Review B* **97**, 235422 (2018).
- [34] F. N. Froning, L. C. Camenzind, O. A. van der Molen, A. Li, E. P. Bakkers, D. M. Zumbühl, and F. R. Braakman, Ultrafast hole spin qubit with gate-tunable spin-orbit switch functionality, *Nature Nanotechnology* **16**, 308 (2021).
- [35] W. M. Weber and T. Mikolajick, Silicon and germanium nanowire electronics: physics of conventional and unconventional transistors, *Reports on Progress in Physics* **80**, 066502 (2017).
- [36] A. Heinzig, S. Slesazeck, F. Kreupl, T. Mikolajick, and W. M. Weber, Reconfigurable silicon nanowire transistors, *Nano letters* **12**, 119 (2012).
- [37] J. Ridderbos, M. Brauns, J. Shen, F. K. de Vries, A. Li, E. P. Bakkers, A. Brinkman, and F. A. Zwanenburg, Josephson effect in a few-hole quantum dot, *Advanced materials* **30**, 1802257 (2018).
- [38] M. Sistani, J. Delaforce, R. B. Kramer, N. Roch, M. A. Luong, M. I. den Hertog, E. Robin, J. Smoliner, J. Yao, C. M. Lieber, *et al.*, Highly transparent contacts to the 1d hole gas in ultrascaled ge/si core/shell nanowires, *ACS nano* **13**, 14145 (2019).
- [39] J. Delaforce, M. Sistani, R. B. Kramer, M. A. Luong, N. Roch, W. M. Weber, M. I. den Hertog, E. Robin, C. Naud, A. Lugstein, *et al.*, Al-ge-al nanowire heterostructure: from single-hole quantum dot to josephson effect, *Advanced Materials* **33**, 2101989 (2021).
- [40] S. Nadj-Perge, S. Frolov, E. Bakkers, and L. P. Kouwenhoven, Spin-orbit qubit in a semiconductor nanowire, *Nature* **468**, 1084 (2010).
- [41] K. D. Petersson, L. W. McFaul, M. D. Schroer, M. Jung, J. M. Taylor, A. A. Houck, and J. R. Petta, Circuit quantum electrodynamics with a spin qubit, *Nature* **490**, 380 (2012).
- [42] J. Ridderbos, M. Brauns, F. K. de Vries, J. Shen, A. Li, S. KoHERE!HERE!!ling, M. A. Verheijen, A. Brinkman, W. G. van der Wiel, E. P. Bakkers, *et al.*, Hard superconducting gap and diffusion-induced superconductors in ge-si nanowires, *Nano letters* **20**, 122 (2019).
- [43] J. Koch, M. Y. Terri, J. Gambetta, A. A. Houck, D. I. Schuster, J. Majer, A. Blais, M. H. Devoret, S. M. Girvin, and R. J. Schoelkopf, Charge-insensitive qubit design derived from the cooper pair box, *Physical Review A* **76**, 042319 (2007).
- [44] A. Blais, R.-S. Huang, A. Wallraff, S. M. Girvin, and R. J. Schoelkopf, Cavity quantum electrodynamics for superconducting electrical circuits: An architecture for quantum computation, *Physical Review A* **69**, 062320 (2004).
- [45] S. Probst, F. Song, P. A. Bushev, A. V. Ustinov, and M. Weides, Efficient and robust analysis of complex scattering data under noise in microwave resonators, *Review of Scientific Instruments* **86** (2015).
- [46] J. Lisenfeld, A. Bilmes, A. Megrant, R. Barends, J. Kelly, P. Klimov, G. Weiss, J. M. Martinis, and A. V. Ustinov, Electric field spectroscopy of material defects in transmon qubits, *npj Quantum Information* **5**, 105 (2019).
- [47] A. Antony, M. V. Gustafsson, G. J. Ribeill, M. Ware, A. Rajendran, L. C. Govia, T. A. Ohki, T. Taniguchi, K. Watanabe, J. Hone, *et al.*, Miniaturizing transmon qubits using van der waals materials, *Nano letters* **21**, 10122 (2021).
- [48] C. Beenakker, Universal limit of critical-current fluctuations in mesoscopic josephson junctions, *Physical review letters* **67**, 3836 (1991).
- [49] P. Winkel, I. Takmakov, D. Rieger, L. Planat, W. Hasch-Guichard, L. Grünhaupt, N. Maleeva, F. Foroughi, F. Henriques, K. Borisov, *et al.*, Nondegenerate parametric amplifiers based on dispersion-engineered josephson-junction arrays, *Physical Review Applied* **13**, 024015 (2020).
- [50] D. Rieger, S. Günzler, M. Spiecker, P. Paluch, P. Winkel, L. Hahn, J. Hohmann, A. Bacher, W. Wernsdorfer, and I. Pop, Granular aluminium nanojunction fluxonium qubit, *Nature Materials* **22**, 194 (2023).
- [51] A. P. Vepsäläinen, A. H. Karamlou, J. L. Orrell, A. S. Dogra, B. Loer, F. Vasconcelos, D. K. Kim, A. J. Melville, B. M. Niedzielski, J. L. Yoder, *et al.*, Impact of ionizing radiation on superconducting qubit coherence, *Nature* **584**, 551 (2020).
- [52] M. Reznikov, M. Heiblum, H. Shtrikman, and D. Mahalu, Temporal correlation of electrons: Suppression of shot noise in a ballistic quantum point contact, *Physical Review Letters* **75**, 3340 (1995).
- [53] A. Kringhøj, B. Van Heck, T. Larsen, O. Erlandsson, D. Sabonis, P. Krogstrup, L. Casparis, K. Petersson, and C. Marcus, Suppressed charge dispersion via resonant tunneling in a single-channel transmon, *Physical Review Letters* **124**, 246803 (2020).
- [54] A. Bargerbos, W. Uilhoorn, C.-K. Yang, P. Krogstrup, L. P. Kouwenhoven, G. De Lange, B. Van Heck, and A. Kou, Observation of vanishing charge dispersion of a nearly open superconducting island, *Physical review letters* **124**, 246802 (2020).
- [55] D. Willsch, D. Rieger, P. Winkel, M. Willsch, C. Dickel, J. Krause, Y. Ando, R. Lescanne, Z. Leghtas, N. T. Bronn, *et al.*, Observation of josephson harmonics in tunnel junctions, *arXiv preprint arXiv:2302.09192* (2023).
- [56] C. Kloeffel, M. Trif, and D. Loss, Strong spin-orbit interaction and helical hole states in ge/si nanowires, *Physical Review B* **84**, 195314 (2011).
- [57] X. Pan, Y. Zhou, H. Yuan, L. Nie, W. Wei, L. Zhang, J. Li, S. Liu, Z. H. Jiang, G. Catelani, *et al.*, Engineering superconducting qubits to reduce quasiparticles and charge noise, *Nature Communications* **13**, 7196 (2022).
- [58] J. Aumentado, G. Catelani, and K. Serniak, Quasiparticle poisoning in superconducting quantum computers, *Physics Today* **76**, 34 (2023).
- [59] A. Houck, J. Schreier, B. Johnson, J. Chow, J. Koch,

J. Gambetta, D. Schuster, L. Frunzio, M. Devoret, S. Girvin, *et al.*, Controlling the spontaneous emission of a superconducting transmon qubit, *Physical review letters* **101**, 080502 (2008).

[60] P. Klimov, J. Kelly, Z. Chen, M. Neeley, A. Megrant, B. Burkett, R. Barends, K. Arya, B. Chiaro, Y. Chen, *et al.*, Fluctuations of energy-relaxation times in superconducting qubits, *Physical review letters* **121**, 090502 (2018).

[61] D. Sabonis, O. Erlandsson, A. Kringhøj, B. Van Heck,

T. W. Larsen, I. Petkovic, P. Krogstrup, K. D. Petersson, and C. M. Marcus, Destructive little-parks effect in a full-shell nanowire-based transmon, *Physical Review Letters* **125**, 156804 (2020).

[62] W. Uilhoorn, J. G. Kroll, A. Bargerbos, S. D. Nabi, C.-K. Yang, P. Krogstrup, L. P. Kouwenhoven, A. Kou, and G. de Lange, Quasiparticle trapping by orbital effect in a hybrid superconducting-semiconducting circuit, *arXiv preprint arXiv:2105.11038* (2021).

Supplemental to Coherent control of a few-channel hole type gatemon qubit

DEVICE OVERVIEW

An optical micrograph of the circuit QED chip is shown in Fig. S1. Four qubits are in the center of the image, capacitively coupled to individual readout resonators (not fully shown). As mentioned in the main text, a 100 nm thick Al layer (bright square) was deposited on the NbTiN ground plane (gray background) as quasiparticle trap. Near the borders of the chip, we deposited a several Au islands for better thermalization.

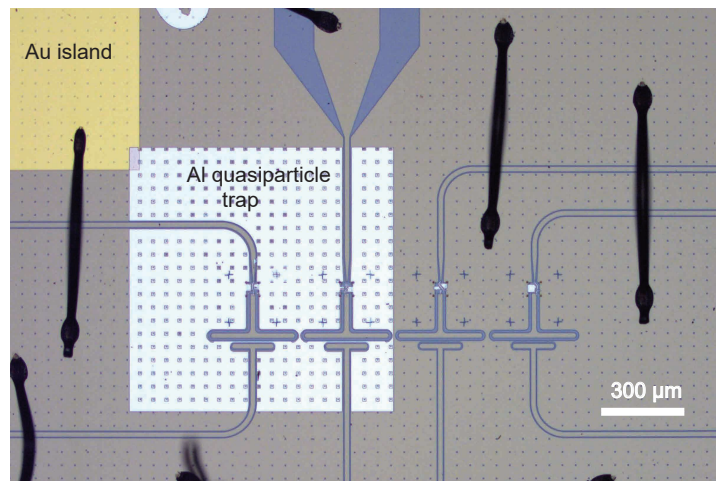


FIG. S1. Optical micrograph of the circuit QED chip. Four qubits were fabricated on each chip (center), coupled to the readout resonator (not fully shown). Al was deposited on the NbTiN ground plane as a quasiparticle trap and Au islands for better thermalization of the chip.

PEAK EXTRACTION

In this section, we elucidate how we extracted the peak positions in the two-tone experiments. The raw data of Fig. 2 (a) is shown in Fig. S2a, with a cross section at $V_g = -30.7$ V in the bottom panel. To better identify the double-peak structure already visible in the raw data, we first applied a moving average with a window size of 10 pixels along the frequency axis, and then took the second derivative. The frequency step size in the raw data is 1 MHz. A cross section of the processed data is displayed alongside the raw data in the lower panel of Fig. S2a.

Next, we extract the peak positions as the positions of the maxima in the second derivative of the smoothed raw data. These positions are pointed out by red dots in the two-tone spectroscopy map in Fig. S2b. We manually discard peaks close to horizontal resonances that we attribute to gate voltage independent two-level fluctuators. From the difference between the two maxima we extract the anharmonicity, as discussed in the main text. Fig. S2c shows additional data and the corresponding second derivative for a different gate voltage range.

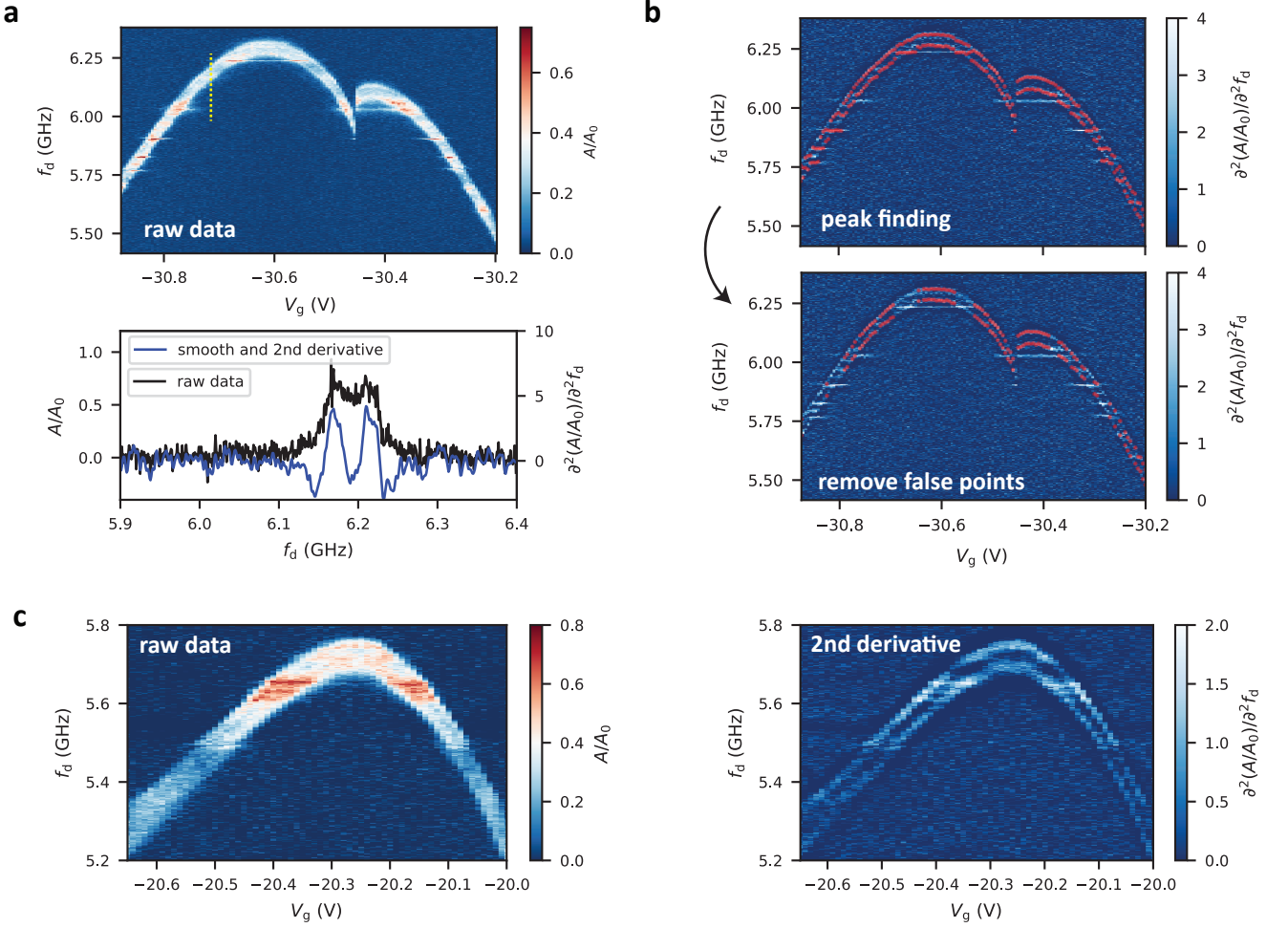


FIG. S2. **Raw data and peak extraction.** **a**, Raw data from Fig. 2a of the main text, showing the two-tone spectroscopy of the gatemon as a function of the drive frequency f_d and the gate voltage V_g . The indicated cross section (yellow dotted line) of raw data and the corresponding processed data are shown in the bottom panel. **b**, Extracted peak positions (red dots) superimposed on the two-tone spectroscopy map. Due to gate-independent spurious resonances, a subset of the peaks was disregarded. Only the ones shown in the bottom panel were used. **c**, Two-tone spectroscopy in a different gate voltage range used for the additional points in the anharmonicity plot of Fig. 2e of the main text. Left panel: raw data, right panel: second derivative of smoothed data.

POWER DEPENDENCE OF THE RABI OSCILLATIONS

In a pure two-level system, the Rabi oscillations are faster for larger power, with a frequency proportional to the drive amplitude, or to the square root of the power. In Fig. S3a, we plot three examples of Rabi oscillations for the indicated (constant) powers. We then extract the Rabi frequency f_{Rabi} by fitting the data points to a sinusoidal function with an exponentially decaying envelope. The resulting f_{Rabi} is plotted as a function of the relative drive amplitude $V_d/V_0 = \sqrt{P/P_0}$ in Fig. S3b. For low amplitudes, f_{Rabi} increases linearly with V_d , as expected. However, for f_{Rabi} larger than ~ 80 MHz, the observed frequency clearly deviates from the low-amplitude linear dependence. This deviation can be directly attributed to transitions to the second excited state of the gatemon, or in other words, to a leaking out of the computational sub-space. This effect can have two physical origins: 1) a larger power results in a larger occupation of the first excited state and therefore to a larger probability of the two-photon processes that drive the $|0\rangle \rightarrow |2\rangle$ transition. 2) drive pulses of short duration result in a broader frequency spectrum, if assuming a Gaussian broadened pulse shape [5], starting to drive the $|1\rangle \rightarrow |2\rangle$ transition [5]. The deviation from the basic low-power linear dependence occurs around ~ 80 MHz, consistent with the anharmonicity found in the main text. This discussion directly illustrates how the anharmonicity limits the qubit operation speed.

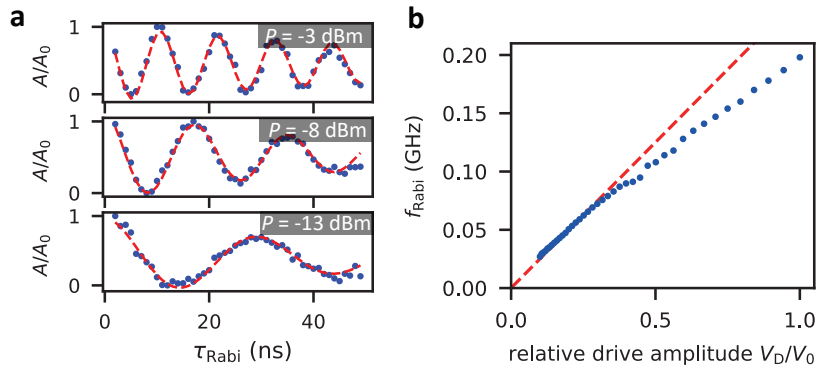


FIG. S3. **Power-dependent Rabi measurements.** **a**, Rabi oscillations at different drive powers $P = -3$ dBm, $P = -8$ dBm and $P = -13$ dBm, as indicated. A sinusoidal function with exponential decay (dashed red line) is fitted to the measured data (blue points) to extract the Rabi frequency f_{Rabi} . **b**, f_{Rabi} as a function of the relative drive amplitude V_D/V_0 . The red dashed line is a linear fit in the low power range.

BEATING PATTERN IN RAMSEY EXPERIMENTS

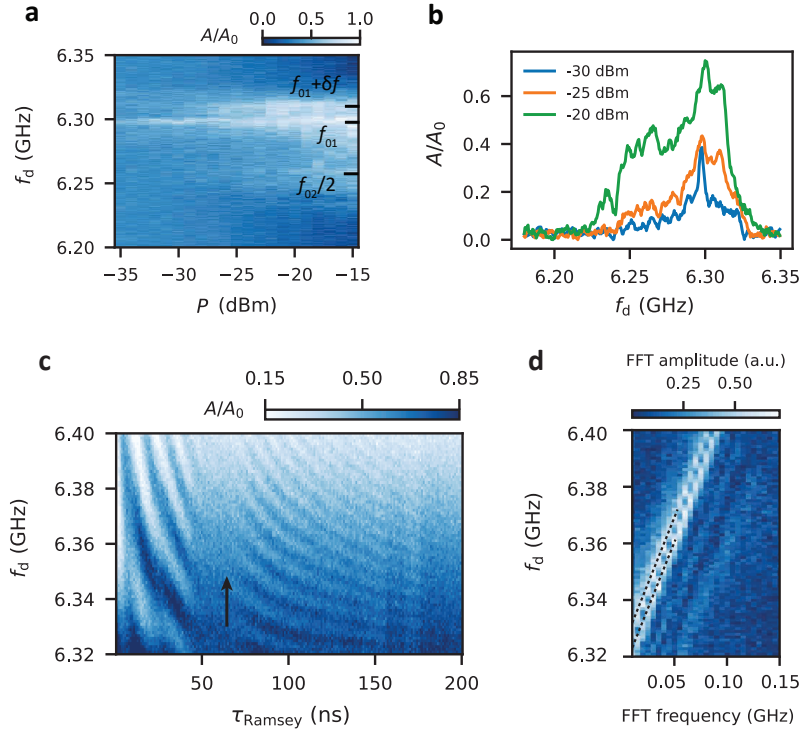


FIG. S4. **Beating pattern in Ramsey measurement.** **a**, Two-tone spectroscopy as a function of drive power P and drive frequency f_d . Specific cross sections at different drive powers are shown in **b**. **c**, Example of a Ramsey type measurement described in the main text. The signal vanishes intermittently around $\tau_{\text{Ramsey}} \sim 70$ ns, pointed out by a black arrow, as discussed in the main text. **d**, Fast Fourier transform of **c** showing two main qubit frequencies, indicated by black dashed lines.

In Fig. S4, a high-resolution power-dependent two-tone spectroscopy experiment is presented. In addition to the resonances at f_{01} and $f_{02}/2$ discussed in the main text, a third transition at a frequency offset δf above f_{01} is visible, with δf ranging from 5 MHz to 10 MHz. We tentatively attribute this resonance to a power dependent fast switching between two slightly different values of f_{01} , which leads to the beating pattern observed in our Ramsey measurements. Figure S4c shows an example in which the beating is clearly visible. The signal vanishes around a delay time of $\tau_{\text{Ramsey}} \sim 70$ ns, and re-appears for higher values. The Fourier transform of these data is shown in Fig. S4d, in which two different frequency components are found close to the main qubit transition f_{01} (dashed lines).

The switching between two qubit frequencies could have various origins. In our case, two possibilities can be excluded: 1) quasiparticle poisoning [57, 58] would block one or more transport channels and therefore change the Josephson energy, and with it the qubit frequency. Since there are only two channels dominating the transport in our JJ (see main text), a poisoning would change the qubit frequency by several GHz, not merely by a few ten MHz as found in our experiments. 2) fluctuations in the Cooper pair number [43] should occur on the kHz, not on the MHz scale, based on the ratio $E_J/E_c \approx 80$. After these consideration, We tentatively attribute the switching frequency to a nearby bi-stable charge fluctuator [22].

RELAXATION AND DEPHASING MECHANISMS

With changes in the gate voltage (and therefore the qubit frequency), T_1 changes seemingly randomly between 0.6 to 1.3 μs . Similar to [9, 23, 26], we cannot find a clear correlation between T_1 and f_{01} or df_{01}/dV_g . Moreover, the obtained T_1 values are much lower than $T_{\text{Purcell}} = 1/(2\pi\kappa(g/\Delta^2)) \approx 100\mu\text{s}$ ($\kappa = 1.5\text{ MHz}$ and $\Delta = 1.5\text{ GHz}$), suggesting that the qubit relaxation time is not limited by the Purcell decay [59] into the readout resonator. We tentatively attribute the gate dependence of T_1 to two-level fluctuators weakly coupled to the qubit, resulting in various energy-relaxation channels [60]. This is supported by the finding that after leaving the device in ambient conditions for several weeks, the average T_1 dropped by a factor of ~ 2 . This suggests that with more impurities adsorbed on the nanowire surface, the qubit energy relaxation time T_1 drops considerably.

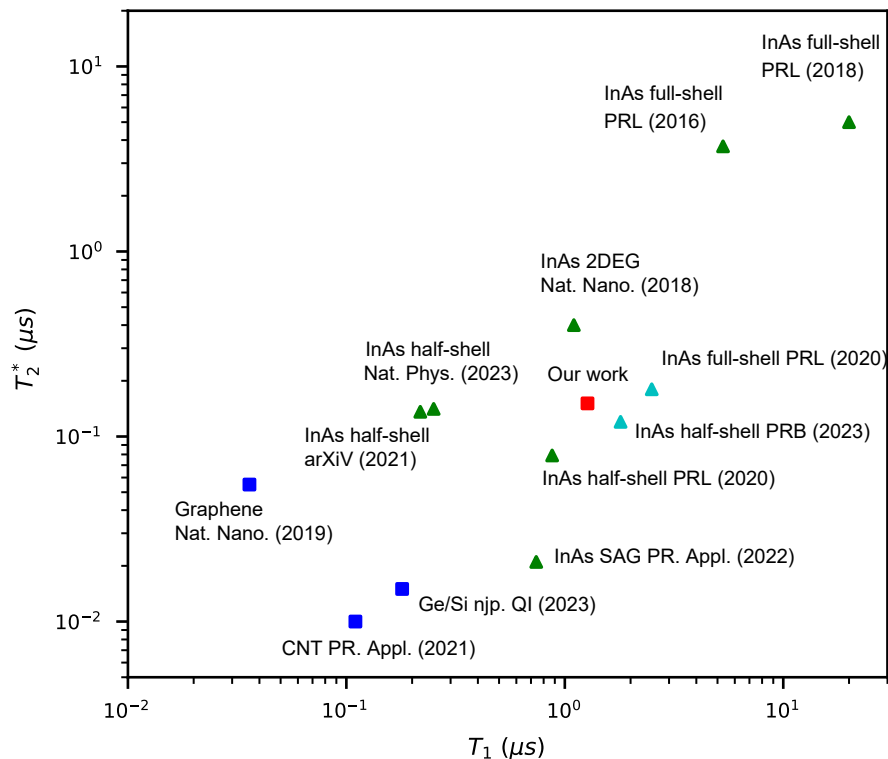


FIG. S5. **Comaprison of transmon coherence times for different material platforms.** The plot shows literature values for T_1 and T_2^* times for various experiments in the literature. Squares symbolize group IV devices, green and cyan triangles stand for III/V InAs-based ones. The cyan data points is a subset of group III/V gatemon experiments in which T_2^* was not reported and we substituted it by T_{Rabi} . The data and the corresponding references are listed in Table S1

In our gatemon, $T_2^* \ll 2T_1$, showing that the qubit coherence is not limited by energy relaxation. In addition, we did not find a significant improvement of T_2^* on and off the gate sweet spots, for example at $V_g \approx -30.6\text{ V}$, nor with better filtering on the DC gate-line by replacing the 80 MHz low-pass LC filters by 100 kHz RC filters. From these findings, we conclude that T_2^* is not limited by gate voltage noise, but rather by on-chip noise originating for example from localized states in the native oxide of the Si shell or in thermal oxide of the substrate, resist residues from fabrication, or from carbon contamination from SEM imaging.

To compare the coherence times of our gatemon to other platforms, we show the results from prior studies in Fig. S5

Material	Platform	Superconductor	T_1 (μ s)	T_2^* (μ s)	$T_{2,echo}$ (μ s)	# channels
III/V	InAs NW (full-shell) [21]	Epitaxy	5.3	3.7	9.5	2 to 3 [12]
III/V	InAs NW (full-shell) [22]	Epitaxy	20	5	30	2
III/V	InAs NW (full-shell) [20]	Epitaxy	0.251	0.141	0.33	
III/V	InAs NW (full-shell) [61]	Epitaxy	0.25	0.18		
III/V	InAs NW (half-shell) [13]	Epitaxy	1.8	0.12		
III/V	InAs NW (half-shell) [62]	Epitaxy	0.218		0.136	
III/V	InAs NW (half-shell) [54]	Epitaxy	0.875	0.079	0.295	
III/V	InAs 2DEG [23]	Epitaxy	1.1	0.4	2.2	many
III/V	InAs SAG NW [24]	Epitaxy	0.74	0.021	1.34	2
IV	Graphene [26]	Surface	0.036	0.055		many
IV	Carbon nanotube [25]	Surface	0.11	(0.01)		1
IV	Ge/Si core/shell thick NW [27]	Al-Ge exchange	0.18	(0.015)		many
IV	Ge/Si core/shell thin NW (our work)	Al-Ge exchange	1.27	0.151		2

TABLE S1. **Comparison of gatemon platforms** The columns in this table show the material (group III/V or group IV), the exact platform, the types of superconducting contacts, the best reported qubit characteristics times T_1 , T_2^* , $T_{2,echo}$, as well as the number of channels active in the JJ. Numbers in brackets indicate that T_2^* was not directly measured in the Ramsey experiment, but deduced from the qubit linewidth. For data points in cyan color, T_2^* were not reported in the experiment, we therefore use T_{Rabi} instead.

and in Table. S1. Our gatemon exhibits the best coherence times of the rather few group IV based platforms to date, on a similar scale as recent InAs based materials with epitaxial Al.

SUPERCONDUCTING GAP MEASUREMENT

The superconducting gap Δ is measured in a control device, shown in Fig. S6a. The device is fabricated with the same annealing method, with a Ge channel length of 250 nm. The device was cooled down in the same dilution refrigerator as the circuit QED chip.

When the NW is gate-tuned close to pinch off, the NW channel forms a quantum dot, tunnel coupled to the annealed Al in the NW. In this regime, we can perform tunnel spectroscopy to determine the superconducting gap Δ . For this, we measured the differential conductance $\partial I_D / \partial V_{SD}$ as a function of source-drain voltage bias V_{SD} and side gate voltage V_{SG} . As shown in Fig. S6b, we find Coulomb blockade diamonds with a gap of 2Δ in the transport opened around zero bias. A cross section at the indicated gate voltage is plotted in Fig. S6c, where we extract $\Delta \approx 210 \mu\text{eV}$.

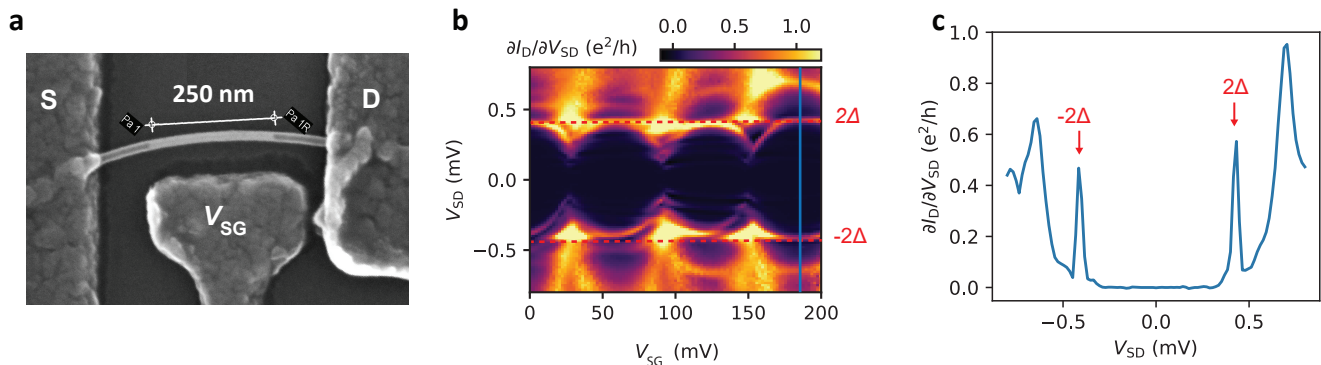


FIG. S6. **Superconducting gap from DC transport.** **a**, SEM image of a Ge/Si core/shell nanowire (NW) JJ fabricated with the same annealing method as in the main text. **b**, DC voltage bias spectroscopy as a function of the gate voltage V_{SG} and the source-drain bias voltage V_{SD} . A cross section at $V_{SG} = 187 \text{ mV}$ is shown in **c**.

RESONATOR QUALITY FACTOR

We use the python based package “resonator_tools” [45] to extract the quality factors of our readout resonator. The data and fits of the magnitude and phase of the transmission signal S_{21} are shown in Fig. S7, yielding the internal

and external quality factors listed in the caption of the figure.

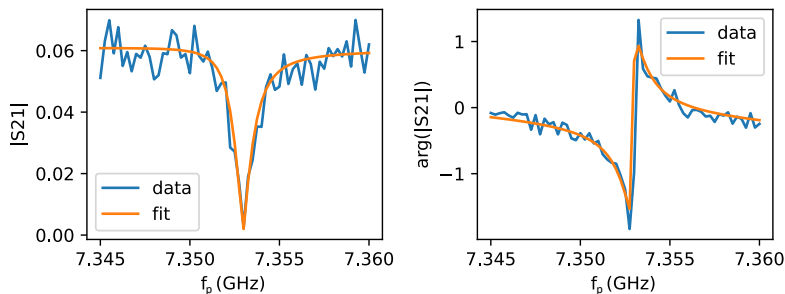


FIG. S7. The measured magnitude and phase of S_{21} in the vicinity of $f_{r,b}$. A simultaneous fit to both quantities using the model in Ref. [45] results in the internal quality factor $Q_i \approx 2.41 \times 10^5$ and the external quality factor $Q_c \approx 4 \times 10^3$.

MEASUREMENT SETUP

The RF measurements were performed either using a Rohde&Schwarz ZNB-8 vector network analyzer or a Zurich Instrument SHFQA Quantum Analyzer. The drive and probe signals were heavily attenuated by 66 dB and filtered with home-made Ecosorb filters at low temperature. The output signals were amplified in an amplification chain consisting of a Josephson parametric amplifier (JPA), several circulators, an Ecosorb filter and dual junction isolators, followed by a HEMT amplifier. All components are shown in detail in Fig. S8.

The qubit drive tone is generated by a vector signal generator (Agilent E8267D) modulated by an envelope signal from an arbitrary waveform generator (AWG, Tektronix 5014C). The DC flux and gate lines are filtered using Ag epoxy filters at the coldplate and a 3-stage LC-filter with the cutoff frequencies 80 MHz, 225 MHz and 400 MHz. The qubit drive via the gate is achieved by combining a DC and an RF line on the PCB with a RC bias tee using a 1 k Ω resistor and a 15 nF capacitor.

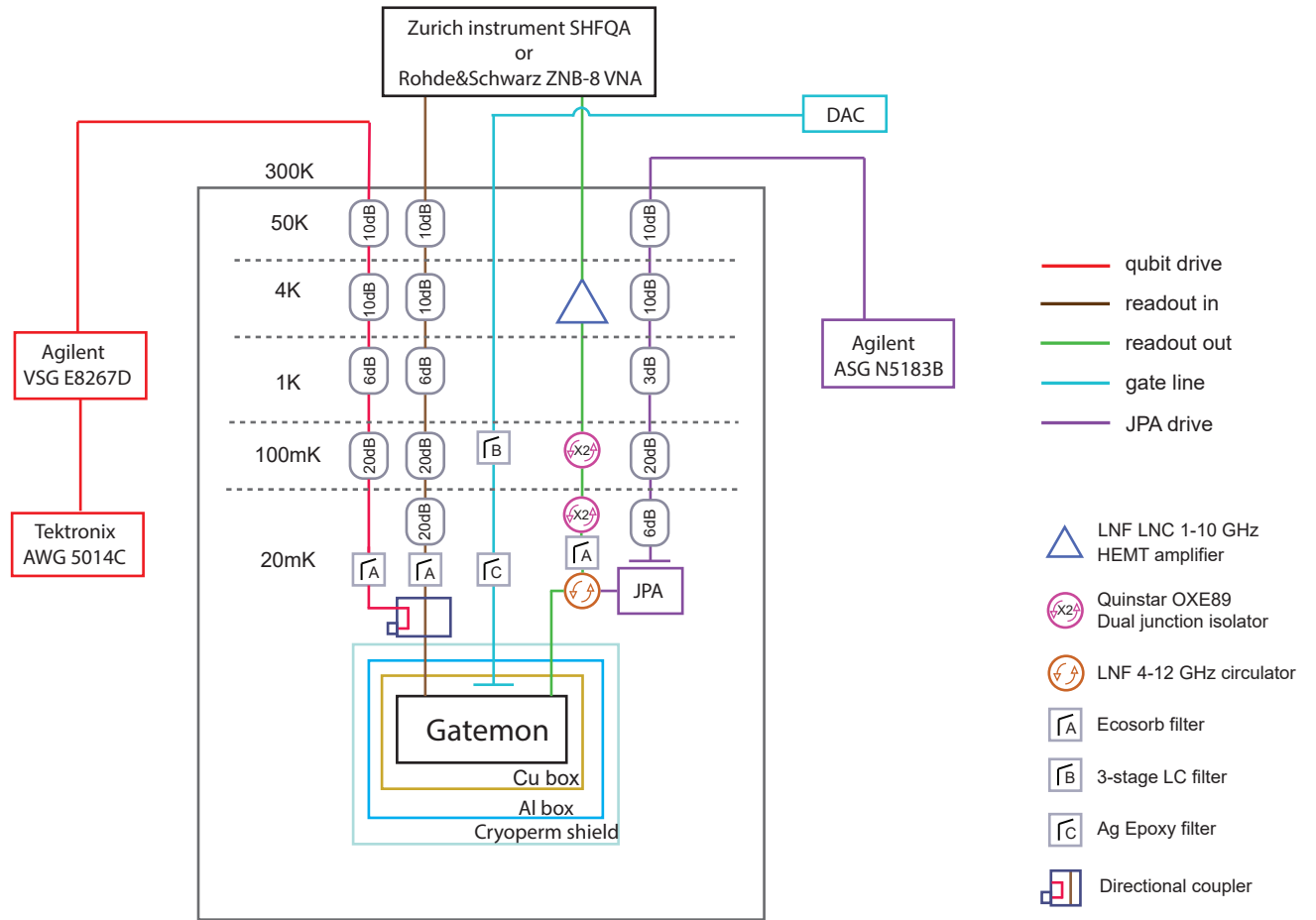


FIG. S8. Schematic of the dilution refrigerator and measurement setup.